Title: Summertime cloud phase strongly influences surface melting on the Larsen C ice shelf, Antarctica

Authors: Gilbert, E.*[1,2]; Orr, A.[1]; King, J. C. [1]; Renfrew, I. A. [2]; Lachlan-Cope, T. [1]; Field, P. F. [3,4]; Boutle, I. A.[3]

[1] British Antarctic Survey, High Cross, Madingley Road, Cambridge CB3 0ET

[2] School of Environmental Sciences, University of East Anglia, Earlham Road, Norwich NR4 7TJ

[3] Met Office, FitzRoy Road, Exeter EX1 3PB

[4] University of Leeds, Leeds, LS2 9JT

* Corresponding author: ellgil82@bas.ac.uk

Funding Information

This work was supported by the Natural Environment Research Council through the EnvEast Doctoral Training Partnership [grant number NE/L002582/1].

Abstract

Surface melting on Antarctic Peninsula ice shelves can influence ice shelf mass balance, and consequently sea level rise. We show that summertime cloud phase on the Larsen C ice shelf on the Antarctic Peninsula strongly influences the amount of radiation received at the surface and can determine whether or not melting occurs. While previous work has separately evaluated cloud phase

and the surface energy balance (SEB) during summertime over Larsen C, no previous studies have examined this relationship quantitatively. Furthermore, regional climate models frequently produce surface radiation biases related to cloud ice and liquid water content. This study uses a high-resolution regional configuration of the UK Met Office Unified Model (MetUM) to assess the influence of cloud ice and liquid properties on the SEB, and consequently melting, over the Larsen C ice shelf. Results from a case study show that simulations producing a vertical cloud phase structure more comparable to aircraft observations exhibit smaller surface radiative biases. A configuration of the MetUM adapted to improve the simulation of cloud phase reproduces the observed surface melt most closely. During a five-week simulation of summertime conditions, model melt biases are reduced to < 2 W m^{-2}: a four-fold improvement on a previous study that used default MetUM settings. This demonstrates the importance of cloud phase in determining summertime melt rates on Larsen C.

Keywords: cloud phase, surface energy balance, Antarctic Peninsula, surface melt, Larsen C ice shelf, regional climate modelling

1. Introduction

Despite their importance in the polar climate system, Antarctic clouds are among the most under-sampled in the world because of the difficulties of in situ data collection in this harsh, remote environment (Lachlan-Cope, 2010; Bromwich et al., 2012). The effect of Antarctic clouds on the amount of energy at the surface (the surface energy balance, SEB) can determine whether the ice surface remains frozen or melts (Kalesse et al., 2016; Nicholas et al., 2017), with consequent implications for ice sheet mass balance and, potentially, for global sea level rise. Cloud impacts on SEB are most important in warmer regions like the Antarctic Peninsula, where surface temperatures

can rise above freezing in summer and cause melting, and where fractional cloud cover is typically 80-90% (Lachlan-Cope, 2010). The recent surface temperature rise and the loss of ice mass on more than half of the Peninsula's ice shelves further motivates investigation of cloud in this region (Turner et al., 2005; 2016; Cook & Vaughan, 2010).

Larsen C is the largest remaining ice shelf on the Antarctic Peninsula, occupying ~47,000 km^2 (Bevan et al., 2017). Previously neighbouring ice shelves, Larsen A and B, collapsed in 1995 and 2002, respectively, largely as a result of atmospherically-driven surface melting (van den Broeke, 2005). Surface melting can destabilise ice shelves via 'hydrofracturing', whereby meltwater percolates into pre-existing rifts and expands, causing crevasses to propagate (Scambos et al., 2000; 2003). Because melt rates are controlled by the balance of surface fluxes, understanding the influence of clouds on the SEB is of great importance to help establish whether Larsen C is likely to suffer the same fate.

Cloud phase strongly influences cloud radiative properties. Mixed-phase clouds dominate in summer over coasts and ice shelves like Larsen C (Lachlan-Cope, 2010; Listowki et al., 2019) and have a complex vertical profile, with multiple thin layers in a 'water-over-ice' structure of supercooled liquid droplets above heavier ice crystals (Barrett et al., 2017). Clouds with higher liquid water paths, comprised of many small droplets, are less transmissive to incoming shortwave radiation, and more emissive in the infrared, so radiate more longwave radiation back to the surface (Zhang et al., 1996). However, the vertical position of liquid within the cloud is important: for instance, the supercooled liquid upper layer of mixed-phase clouds can reflect lots of shortwave radiation, but has little effect on longwave emission (Barrett et al., 2017).

Atmospheric models typically struggle to represent cloud phase or vertical structure correctly, especially at high latitudes. For example, Klein et al. (2009) find that models cannot usually simulate enough liquid water in Arctic stratocumulus because too much ice is formed at the expense of

supercooled liquid. Many atmospheric models, including the UK Met Office Unified Model (MetUM) used in this study, exhibit this bias in cloud phase and structure because their microphysical parameterisations are developed for the mid-latitudes and are relatively simple. For example, poor representations of processes like riming (Furtado et al., 2016) and vapour deposition (Furtado & Field, 2017), as well as large-scale cloud phase partitioning (Abel et al., 2017) have been shown to cause the MetUM to over-estimate cloud ice and under-estimate cloud liquid contents. In many models, errors in cloud phase produce significant SEB biases, most notably over the Southern Ocean (Bodas-Salcedo et al., 2012; Hyder et al., 2018). This is because sub-grid scale spatial variability in temperature and humidity are necessarily parameterised in the model by large-scale cloud schemes, which compute liquid and ice cloud fractions that are then fed into the microphysics scheme. In reality, ice and liquid can co-exist in spatially segregated pockets (Tan & Storelvmo, 2016), but in the MetUM it is difficult to sustain a separation between the phases. When total cloud fraction exceeds 100%, ice and liquid phases are assumed to overlap within a homogeneously mixed mixed-phase region. In this mixed-phase region, ice forms preferentially because of the lower saturation vapour pressure over ice than liquid.

Modelled cloud has been implicated as a primary driver of surface radiation biases over Antarctica (Bromwich et al., 2013; Lenearts et al., 2017) and specifically over Larsen C (King et al., 2015; Listowski & Lachlan-Cope, 2017). King et al. (hereafter K15) find that three different regional atmospheric models simulate either too little cloud, or cloud that is optically too thin over the ice shelf. Summertime clouds over Larsen C in the MetUM are optically too thick in the shortwave part of the spectrum, while being too thin in the infrared, which results in negative downwelling shortwave ($SW_{\downarrow}$) and longwave ($LW_{\downarrow}$) biases. Overall, they find positive (negative) net shortwave (longwave) fluxes that do not entirely cancel, which produces a positive net energy flux at the surface and can cause the MetUM to over-estimate melt on Larsen C. High resolution regional climate models are typically able to represent the radiative effects of mixed-phase cloud more

accurately than global models (Vergara-Temprado et al., 2018). However, computational constraints still necessitate parameterisations that approximate sub-grid scale cloud properties, which produce errors in the SEB. Both Listowski & Lachlan-Cope (2017) and Hines et al. (2019) use the Polar-WRF model (and AMPS, in the case of Hines et al.) to show that more sophisticated parameterisations produce more accurate simulations of cloud microphysical properties, and consequently surface radiative fluxes, over Larsen C and the West Antarctic, respectively. Both find that double-moment parameterisations of liquid water represent cloud and SEB properties most accurately.

Over the entire continent, the widely varying representations of cloud phase between models and re-analyses still produce considerable errors in radiative fluxes: generally, CMIP5 models under-estimate $SW_{\downarrow}$ and over-estimate $LW_{\downarrow}$ (Lenaerts et al., 2017). A better understanding of phase in Antarctic mixed-phase clouds, particularly the occurrence of supercooled liquid water (e.g. Listowski et al., 2019), is essential to address this problem. For example, an improved cloud scheme was shown to reduce Antarctic-wide SEB biases in RACMO2 (van Wessem et al., 2014), and to increase modelled melt and precipitation rates over the Antarctic Peninsula (van Wessem et al., 2018). Melt and precipitation are both key inputs to surface mass balance (SMB) calculations so improving simulated cloud phase and radiative effects contributes to a better understanding of SMB and consequently sea level rise. This is particularly important in coastal Antarctica (including the peninsula), where melt and precipitation rates are high, and model SEB biases are largest (Lenaerts et al., 2017). Antarctic SMB has been estimated using regional models like MAR (Agosta et al., 2018), COSMO-CLM^2 (Souverijns et al., 2019) and RACMO2 (Lenaerts et al., 2018; van Wessem et al., 2018), but further work is still required to better constrain modelled SMB. For instance, RACMO2 still over-estimates coastal orographic precipitation rates near the grounding line of west Antarctic glaciers partly due to its representation of cloud (Lenaerts et al., 2018).

There is currently a gap in scientific understanding on the influence of cloud phase on the SEB and melting over Antarctic Peninsula ice shelves. This has wider implications for model estimates of SMB across Antarctica, and therefore sea level rise. K15 conclude that cloud properties are a likely cause of observed SEB biases. However, although observed cloud phase on the peninsula has been assessed by Grosvenor et al. (2012) and Lachlan-Cope et al. (2016) and modelled by Listowski and Lachlan-Cope (2017), no work has been done to explicitly connect these properties to the SEB. This study will address this gap by investigating the sensitivity of the SEB to simulated cloud phase in a high-resolution regional climate configuration of the MetUM.

2. Data and Methods

2.1 Study Area

The study focuses on Larsen C, an ice shelf with a flat, homogenous surface on the eastern side of the mountains that extend approximately north-south along the Antarctic Peninsula (Figure 1). During summer, the shelf is characterised by relatively low wind speeds, high relative humidity and cloudy conditions (Kuipers Munneke et al., 2012).

2.2 Data

Two observational datasets are used to validate MetUM-simulated cloud phase and SEB over Larsen C. Namely, airborne observations of cloud collected with the British Antarctic Survey's instrumented Twin Otter aircraft and observations of surface meteorology and energy fluxes from an automatic weather station (AWS14), located at 67°00.8'S 61°28.8' W at 40 m above sea level. These data are from the Orographic Flows and Climate of the Antarctic Peninsula (OFCAP) campaign which took place between January 1 and February 7, 2011 (see Elvidge et al. 2015; 2016 and K15).

142 The aircraft measures standard meteorological variables like temperature, pressure and humidity,
143 three dimensional winds and up- and downwelling radiation. A DMT Cloud, Aerosol and
144 Precipitation Spectrometer (CAPS probe, Baumgardner et al., 2001) containing three separate
145 instruments to sample cloud particles of different sizes was also fitted. A full description of aircraft
146 observations and data treatment can be found in Grosvenor et al. (2012), Lachlan-Cope et al. (2016)
147 and Appendix A.

148 AWS14 measures near-surface meteorology and radiation components directly. Turbulent fluxes are
149 computed using the bulk aerodynamic method to retrieve the full SEB, and the energy balance model
150 of van den Broeke et al. (2005) calculates the SEB of the snowpack. Further details of weather
151 station measurements and data treatment are given in Kuipers Munneke et al. (2009; 2012) and
152 Appendix B.

153 The SEB of the ice surface is defined as per K15 and summarised as:

154 $$E_{tot} = SW_{net} + LW_{net} + H_L + H_S \quad (1)$$

155 where SW_{net} and LW_{net} are the net (downwelling minus upwelling) shortwave and longwave fluxes,
156 respectively; and H_L and H_S are the surface latent and sensible heat fluxes, respectively. Melting
157 occurs when the sum of fluxes, E_{tot}, is positive, and the surface temperature, T_s, is at the melting
158 point: 0°C. Energy available for melting (or melt flux, E_{melt}) is therefore equal to E_{tot} when T_s = 0°C,
159 as described in K15. All fluxes, including E_{melt} and E_{tot}, are measured in W m^{-2} and are positive when
160 directed towards the surface.

161

162 ## 2.2 Model description

163 The MetUM (Walters et al., 2017) is a non-hydrostatic numerical weather prediction model that uses
164 semi-implicit time-stepping and semi-Lagrangian advection. A regional configuration using RA1

165 science settings was run in atmosphere-only forecast mode, with a setup adapted from Orr et al.
166 (2014) and forecast length of 24 hours. It was run in a nested configuration with a 1.5 km resolution
167 inner domain centred on the Larsen C ice shelf, shown in Figure 1. This domain is positioned within
168 a global domain that has ~17 km resolution at mid-latitudes (N768) and was initialised with global
169 UK Met Office operational analyses. The MetUM radiation scheme is based on Edwards & Slingo
170 (1996) and all experiments used the operational single-moment cloud microphysics scheme based on
171 Wilson & Ballard (1999), with extensive modifications as described in Bush et al. (2019). The
172 heterogeneous ice nucleation temperature threshold (representing an immersion freezing or
173 condensation mechanism, whereby ice is permitted to form heterogeneously in the presence of liquid
174 water) used by the microphysics scheme was changed from its default value of -10°C to -18°C,
175 shown by Field et al. (2014) to improve the representation of mixed-phase cloud. Additional details
176 of model parameterisations are given in Appendix C.

177

178 ### 2.3 Method

179 Cloud properties and surface fluxes are examined in detail during one instructive case study (flight
180 152, hereafter referred to as f152, conducted on January 18, 2011). This flight was selected because
181 the aircraft conducted two vertical profiles between 100 and 5000 m near AWS14. The flight track
182 and location of AWS14 are shown in Figure 1. Observed and modelled surface fluxes and in-cloud
183 vertical profiles are compared at AWS14 during f152. Model output is taken from the closest
184 gridpoint to AWS14's location, plus the eight surrounding gridpoints: an area of approximately 4.5
185 km^2. Because AWS14 is located on a flat, homogeneous ice surface, it can be reasonably assumed
186 that conditions there are representative of a large area (K15). Mean vertical profiles are computed
187 from observations and model output using in-cloud data only, during the period when the aircraft

was sampling over the ice shelf (approximately 1500-1700 UTC). Further detail is given in the appendices.

Four model experiments were run with varying 'Regional Atmosphere' (RA) configurations (Table 1). Two sets of RA physics were tested: RA1M and RA1T, configured for the mid-latitudes and tropics, respectively, and described in Bush et al. (2019). These two experiments are the 'base' configurations. The primary differences between them is that RA1M uses the operational (diagnostic) large-scale cloud scheme based on Smith (1990), whereas RA1T uses a prognostic scheme, PC2 (Wilson et al., 2008). Smith (1990) parameterises sub-grid scale variations in humidity and temperature to calculate cloud fractions using a triangular probability distribution function. Condensation within a gridbox occurs when relative humidity reaches a critical value, RH_{crit}, which is specified for each model layer. Cloud liquid and ice fractions (that is, the fraction of the gridbox occupied by liquid or ice cloud) are calculated by the scheme from the liquid and ice contents, before this information is fed into the microphysics for further calculation of cloud properties. The PC2 scheme is prognostic and computes liquid, ice and mixed-phase cloud fractions, which are advected in space and time after updating them by calculating sources and sinks of condensate. Incremental condensate fractions are outputted following each physical process represented by the model, such that each scheme (convection, radiation etc.) must produce an effect on condensate fractions. The connection to the microphysics scheme is slightly adapted compared to Smith (1990), so that autoconversion does not affect liquid cloud fractions. In practice, this permits the existence of extensive, optically thin liquid clouds, with high liquid cloud fraction but low liquid water contents.

The second two experiments (RA1M_mod and RA1T_mod) applied modifications to the base configurations shown to improve the simulation of cold mixed-phase clouds by increasing the supply of liquid water and reducing its conversion to ice (see Table 1 for a summary). These are: (1) the inclusion of shape-dependent riming (Furtado & Field, 2017), (2) the turbulent production of supercooled liquid (Furtado et al., 2016, RA1T only), and (3) modifications to the ice cloud fraction

parameterisation described in Abel et al. (2017) (RA1M only). Firstly, riming depletes liquid water, so limiting the efficiency of this process can sustain higher liquid fractions in mixed-phase clouds. Reducing riming efficiency has been shown to improve Southern Ocean downwelling shortwave radiation biases associated with the conversion of too much cloud liquid water to ice (Furtado & Field, 2017). Secondly, cloud liquid water can also be produced by sub-grid scale variations in humidity that are related to unresolved turbulence. Because turbulent motions occur at finer scale than the MetUM can explicitly resolve, this can produce humidity distribution differences that are also not directly simulated. Furtado et al. (2016) demonstrated that increasing the supply of liquid in this manner can enhance the amount of cloud liquid. This modification is only compatible with the PC2 cloud scheme, on which RA1T is based. Finally, several studies show that ice cloud fractions are consistently over-estimated in mixed-phase clouds by the MetUM (e.g. Field et al., 2014; Abel et al., 2017) due to computational limitations that mean that the model cannot explicitly resolve small-scale spatial heterogeneity in cloud water phase. Abel et al. (2017) develop an adaptation to the ice cloud fraction parameterisation that limits the overlap between the liquid and ice fractions, thereby reducing the conversion of liquid to ice via vapour deposition and riming. This adaption mimics the real-world existence of spatially discrete (sub-grid scale) pockets of ice and liquid without explicitly resolving them. It is only compatible with the RA1M scheme.

The case study was simulated with all four model configurations, then the best-performing configuration was used to simulate the entire five-week OFCAP period. During OFCAP, only the representation of surface fluxes is assessed because cloud phase measurements are not consistently available throughout the period. Initial tests showed modelled cloud phase to be sensitive to forecast length, so the first 12 hours of each 24-hour forecast were discarded as spin-up. The case study simulation was initialised at 00Z on January 18, 2011 to allow the model to spin up. For the longer OFCAP simulation, forecasts were re-initialised every 12 hours and the t+12 to t+24 hour part of each successive forecast was concatenated to form a continuous time series.

3. Results and discussion

3.1 Model representation of case study f152

Observed ice and liquid mass mixing ratios during case f152 (January 18, 2011) over AWS14 indicate that many thin cloud layers are present, with clouds below 2 km exhibiting the 'water-over-ice' structure typical of low-level polar mixed-phase clouds (Figure 2). A higher altostratus layer is present at around 4 km altitude, while a stratocumulus deck is observed between approximately 400 m and 2200 m. This stratocumulus appears in two distinct layers and contains higher mass mixing ratios of cloud ice and liquid than the upper level altostratus, reaching 1.6×10^{-2} g kg^{-1} and 3.4×10^{-1} g kg^{-1}, respectively. While the MetUM successfully captures the presence of altostratus and lower stratocumulus layers, all four model configurations simulate the lowest cloud layer around 1 km higher than is observed and produce just one layer below 2 km rather than the two indicated by the observations.

Figure 2 shows that all model configurations (RA1M, RA1M_mod, RA1T and RA1T_mod) over-estimate ice mass mixing ratios, and under-estimate liquid mass mixing ratios above 2.5 km altitude, where virtually no liquid is present in any configuration. Ice cloud is concentrated in the upper layers (above ~3 km) because any supercooled liquid present is converted readily to ice below the ice nucleation temperature threshold of -18°C. At 4 km altitude, the largest positive bias in ice contents is in RA1T_mod, which produces an ice mass mixing ratio 22.7 times larger than observed, while RA1M shows the smallest bias: an over-estimate of 2.3 times. All models except RA1T_mod produce liquid mass mixing ratios of less than 5.0×10^{-4} g kg^{-1} above 4 km, although liquid mixing ratios are observed to reach 5.3×10^{-2} g kg^{-1} at 3.8 km. At lower altitudes modelled cloud generally contains less liquid and ice than observed. Between 1 and 2 km, ice mass mixing ratios in RA1M_mod peak at 7.2×10^{-3} g kg^{-1}, 1.9 times higher than RA1M, and 2.8 and 7.5 times larger than

in RA1T and RA1T_mod, respectively. At the same height, liquid mass mixing ratios peak in RA1M and RA1M_mod at 1.1×10^{-1} g kg^{-1} and 2.5×10^{-1} g kg^{-1}, respectively, and at 2.1×10^{-3} g kg^{-1} and 5.2×10^{-2} g kg^{-1} respectively in RA1T and RA1T_mod. Overall, ice mass mixing ratios are over-estimated (by between 1.7 times in RA1M and 5.1 times in RA1T_mod), while liquid mass mixing ratios are under-estimated (by 3.0 times in RA1M_mod to 64.9 times in RA1T). This is consistent with the results of Furtado et al. (2016) and Abel et al. (2017) who find that riming and vapour deposition occur too efficiently in modelled cold mixed-phase clouds, forming ice too readily at the expense of supercooled liquid.

The mid-latitude configuration of the model, RA1M, simulates cloud ice and liquid mass mixing ratios that are closer to those observed than the tropical configuration, RA1T. RA1T produces little liquid cloud compared to observations, evident from Figure 2b), and compared to RA1M, shown in Figure 2b) and d). Additionally, RA1T only simulates thin ice clouds over AWS14. This is suggested by Figure 2c), which shows that ice cloud volume fraction reaches 100% at 1.2 km, and Figure 2a), which shows very low ice mass mixing ratios in this layer. Modelled 'volume fractions' refer to the fraction of a gridbox occupied by cloud of each phase: volume fractions in Figure 2 are shown as means for each model layer. RA1T is designed for use in tropical, convective regions and is less suited to Antarctic conditions where convection is less vigorous, which may explain these differences.

Modifications to the 'base' model configurations produce varying results. Observed liquid mass fractions in the lowest simulated cloud layer peak at 3.4×10^{-1} g kg^{-1}. At 2.5×10^{-1} g kg^{-1}, RA1M_mod produces 2.3 times more liquid than RA1M in the lowest layer, but the modifications to RA1M do not change its height, which is still approximately 1 km too high in RA1M_mod. RA1T_mod generates 1.7 times more cloud ice above 3 km than RA1T, but is the only configuration to simulate liquid at this height, as is observed (Figure 2d). Throughout the profile, it also produces almost ten times as much liquid than RA1T, but liquid mass fractions in RA1T_mod are still around

six times lower than in observations. Of all four experiments, RA1M_mod exhibits the lowest bias in liquid mass fractions, while RA1M over-estimates ice mass fractions by the smallest amount.

Specific humidity, i.e. water vapour mass fraction, is represented reasonably accurately (within 10-25% of observed values) in all experiments throughout the profile up to 2 km (not shown). However, between 2 and 3.5 km, modelled water vapour mass fractions are considerably lower than observed (by 63-65% at 2.6 km). This under-estimation of water vapour may be expected to negatively bias longwave fluxes. However, very few differences are detectable between configurations, so this effect should have the same effect on the SEB in all experiments.

Surface flux biases at AWS14 for each model experiment during f152 are presented in Table 2. Energy available for melting, E_{melt}, is over-estimated by all configurations of the MetUM, but the bias is highest in RA1M at 17.33 W m^{-2}, causing modelled E_{melt} to be too large by 37%. Because the modelled and observed surface temperature are at melting point throughout the flight (not shown), this bias is solely driven by errors in the simulated surface fluxes. Additionally, the modelled surface albedo ($SW_{\uparrow}$ / $SW_{\downarrow}$) is within ± 2% of observed values in all simulations, suggesting that biases are driven almost entirely by downwelling radiative errors, and highlighting the importance of cloud phase in determining melt. Net shortwave fluxes (SW_{net}) are simulated better by the two mid-latitude experiments, with the lowest bias produced by RA1M_mod (-1.80 W m^{-2}), while the smallest bias in net longwave (-4.68 W m^{-2}) is found in RA1T_mod. Both modified experiments produce lower shortwave flux biases than their respective 'base' configurations, but RA1M produces smaller $LW_{\downarrow}$ and LW_{net} biases than RA1M_mod.

Between-experiment differences in downwelling fluxes are partly driven by the representation of cloud. Positive $SW_{\downarrow}$ biases in all experiments indicate that the cloud is optically too thin in this part of the spectrum, thus allowing too much solar radiation to reach the surface (as also found by K15). Conversely, over-estimated $LW_{\downarrow}$ indicates that the cloud is optically too thick in the infrared, which

311 can be related to cloud liquid water content, temperature or altitude (Zhang et al., 1996). The lowest
312 simulated cloud layer is approximately 1 km too high in all experiments, while temperature profiles
313 are represented well compared to observations (not shown). A higher cloud base would be expected
314 to contribute to negative $LW_{\downarrow}$ and LW_{net} biases in all experiments, but this is only true of the two
315 RA1T experiments, suggesting a role for other effects, such as biases in parameterised cloud particle
316 size. RA1T_mod exhibits the smallest $LW_{\downarrow}$ bias, while RA1T has the largest. $LW_{\downarrow}$ biases are
317 positive in the two RA1M experiments, and negative in the RA1T experiments, although $LW_{\downarrow}$ and
318 $LW_{\uparrow}$ biases are both comparatively small in RA1T_mod. Positive $LW_{\downarrow}$ biases in RA1M and
319 RA1M_mod are also likely a result of errors in simulated cloud phase, which are only partly offset
320 by negative water vapour biases (not shown). Thick ice clouds can have a significant longwave
321 warming effect (Miller et al., 2015), so although specific humidity and liquid contents - usually the
322 dominant component of cloud longwave radiative forcing – are under-estimated, the considerable
323 over-estimation of ice contents at altitudes above 3 km likely explains this positive bias.

324 The RA1T experiment produces quite different cloud profiles, and consequently SEB biases, to the
325 other three simulations. As shown in Figure 2, RA1T produces very low liquid cloud fractions and
326 virtually no liquid water throughout the cloud profile, which likely explains the negative $LW_{\downarrow}$ (-
327 41.13 W m^{-2}) and extremely positive $SW_{\downarrow}$ (195.38 W m^{-2}) biases shown in Table 2. The amount of
328 shortwave radiation transmitted through ice clouds is relatively insensitive to ice cloud thickness
329 (Miller et al., 2015), which means that although RA1T simulates an ice cloud gridbox volume
330 fraction of 100% in two layers (Figure 1c) and d)), this has a limited effect on surface $SW_{\downarrow}$ because
331 solar radiation can still penetrate. RA1T produces a melt flux bias comparable to RA1M_mod
332 because its large radiative biases cancel and biases in the turbulent fluxes are relatively minor.

333 RA1T_mod has the smallest $LW_{\downarrow}$ bias, but this may be due to errors in simulated cloud phase. A
334 positive $SW_{\downarrow}$ bias indicates that too little (liquid) cloud is simulated (also suggested by the low liquid
335 water contents and volume fractions in Figure 2), which would usually be associated with a large

336 negative $LW_{\downarrow}$ bias. However, cloud occupies up to 80% of the gridbox in the lowest layer, despite
337 the liquid water contents being far too low, suggesting that the layer is extremely thin. Optically thin
338 liquid clouds have been shown to cause greater warming than thicker liquid clouds in summer over
339 the Greenland ice sheet because they are thin enough to allow shortwave radiation to penetrate, but
340 thick, low and warm enough to radiate strongly in the infrared (Bennartz et al., 2013). Errors in
341 simulated cloud phase may therefore produce small biases for the wrong reasons.

342 Overall, RA1M_mod is considered to be the best-performing experimental configuration with
343 respect to cloud and SEB properties. Erroneous cloud fields and large cancelling radiative flux errors
344 remove RA1T and RA1T_mod from consideration. RA1M and RA1M_mod have comparable net
345 longwave biases, and although cancelling $SW_{\downarrow}$ and $SW_{\uparrow}$ errors exist in both, these are smaller in
346 RA1M_mod, which over-estimates $SW_{\downarrow}$ by just 5%. Further, RA1M_mod's E_{tot} and E_{melt} biases are
347 the smallest of all configurations. RA1M_mod is therefore used to run a five-week simulation of the
348 OFCAP period for a second evaluation of simulation quality.

349

350 ### 3.2 Model representation of the OFCAP period

351 Errors in cloud phase have been shown to contribute to errors in downwelling fluxes during flight
352 152. However, because aircraft observations of cloud properties are not available for the entire
353 period, a similar analysis is not possible for OFCAP. Downwelling fluxes are therefore used to infer
354 information about cloud phase during OFCAP. Pearson correlation coefficients are used to
355 understand relationships between melting and observed fluxes (Table 3, Figure 3).

356 Table 3a and Figure 3 show positive correlations (significant at the 99% level) between observed
357 E_{melt} and $SW_{\downarrow}$ ($r_{SW,\,melt} = 0.62$, Figure 3a) and $LW_{\downarrow}$ ($r_{LW,\,melt} = 0.24$, Figure 3b)). This indicates that
358 melt is most likely to occur when more shortwave radiation can reach the surface, but is also weakly
359 associated with higher $LW_{\downarrow}$, which is strongly related to liquid water contents, especially at the

relatively low liquid water paths (< 40 g m^{-2}) typical of Antarctic clouds (Grosvenor et al., 2017). Observed melt is not strongly related to cloud cover ($r_{CC,\ melt}$ = 0.12), and the negative correlation between $SW_{\downarrow}$ and cloud cover shows that $SW_{\downarrow}$ is highest during clear conditions ($r_{CC,\ SW}$ = -0.19), which occur 11.5% of the time (defining 'clear' as having cloud cover < 0.31, as in Kay et al., 2008). The low observed correlation between cloud cover and melt may be explained by the competing effects of cloud longwave (positive correlation) and shortwave (negative correlation) radiative effects on melt. Observed cloud cover is not compared with $LW_{\downarrow}$ because it is computed from the closure of the longwave radiation budget using the energy balance model of Kuipers Munneke et al. (2009) and so is not independent. Modelled relationships (Table 3b) compare well with observations, suggesting that the model is able to reproduce the observed drivers of melting. For example, modelled E_{melt} is positively correlated with $SW_{\downarrow}$ ($r_{SW,\ melt}$ = 0.65) and to a much lesser extent, $LW_{\downarrow}$ ($r_{LW,\ melt}$ = 0.15). Additionally, the large and significant (at the 99% level) correlation between modelled cloud cover and $LW_{\downarrow}$ ($r_{CC,\ LW}$ = 0.87) suggests that cloud cover affects longwave fluxes most strongly in the MetUM. This is mostly due to the contribution of liquid clouds – the correlation between $LW_{\downarrow}$ and liquid water path is much higher ($r_{LWP,\ LW}$ = 0.63) than with ice water path ($r_{IWP,\ LW}$ = 0.21) (not shown). Modelled melting during OFCAP usually follows cloudy periods, during which liquid and then ice water paths increase and then rapidly decline as cloud glaciates and dissipates (not shown). Higher cloud liquid water contents increase $LW_{\downarrow}$ and begin to increase surface temperature and E_{tot}. Melting first begins as $LW_{\downarrow}$ increases, but is then sustained as the cloud glaciates and more shortwave radiation can reach the surface. This time-evolving process may partly explain the relatively low modelled correlations with melt of cloud cover and downwelling fluxes.

Biases in modelled SEB terms during the OFCAP period (Table 4) are smaller than those reported by K15, who use an earlier version of the default MetUM configuration, and broadly similar to those during f152 (Table 2). As in f152, SW_{net} is negatively biased, but not for the same reasons: whereas during f152 $SW_{\downarrow}$ is positively biased, during OFCAP it is negatively biased, indicating that cloud is

385 optically too thick in the shortwave part of the spectrum during the OFCAP period. This finding is
386 consistent with K15. Mean longwave biases are all ~1 W m^{-2} in magnitude, but $LW_{\downarrow}$ (and
387 consequently LW_{net}) shows a poor correlation with observations, indicating that the model struggles
388 to represent (liquid) clouds, atmospheric water vapour contents and/or that clouds are simulated at
389 the wrong time. This is consistent with results from the case study, which shows that the MetUM
390 represents some cloud properties poorly. For example, errors in simulated cloud base height may
391 explain the poor correlation with observed $LW_{\downarrow}$, as seen for the f152 case, when the MetUM-
392 simulated cloud base was 1 km too high.

393 As shown in Table 4, modelled radiative biases during OFCAP are mostly of the same sign as K15,
394 but smaller in magnitude, suggesting that the MetUM physics updates since 2015 and modifications
395 made in this work have improved the representation of cloud microphysics, and consequently surface
396 energy fluxes. The melt flux bias is smaller than in K15 and during f152 (-1.7 W m^{-2} compared to 7.6
397 W m^{-2} in K15 and 6.09 W m^{-2} in f152, an under-estimate of just 12%), but of the opposite sign. This
398 results in a 13% under-estimate of cumulative meltwater production throughout OFCAP, at 114 mm
399 (water equivalent). K15 found that the MetUM over-predicts the occurrence of melt, despite a cold
400 bias that is particularly present at high latitudes where conditions are more stable (Lock, 2011).
401 Although the OFCAP simulation also produces a small mean cold bias (-0.27°C), and exhibits
402 considerable negative biases in surface temperature during night-time, it represents melt frequency
403 well because errors in modelled surface temperature are mostly when it is already well below the
404 melting point (Figure 4). Observed melting occurs 29.5% of the time during OFCAP, while the
405 model simulates melting 32% of the time. E_{melt} biases are therefore smaller than E_{tot} biases because
406 melt occurs only when the surface temperature is at melting point. Remaining biases, for instance in
407 the turbulent fluxes, may be explained by other sources of error, such as the land surface or
408 boundary-layer schemes. Improvements made in the RA1M_mod configuration produce much better
409 simulations of melt at AWS14 than the present default configurations and previous model versions.

Because surface fluxes at AWS14 are representative of a wider area (K15) and the large-scale meteorological forcing producing cloud is similar across the ice shelf, these improvements will likely be seen across the whole of Larsen C.

4. Conclusions

This study has shown that the representation of cloud phase in the MetUM strongly influences modelled summertime surface energy fluxes and melt over the Larsen C ice shelf. An optimum configuration, RA1M_mod, is identified and recommended for future work examining cloud properties and surface energy fluxes over the Antarctic Peninsula. RA1M_mod uses single-moment microphysics and is based on the MetUM's mid-latitude regional atmosphere package, including modifications proposed by Furtado & Field (2017) and Abel et al. (2019). These adaptations to improve simulated cloud phase have wider applications for other regional models and in other regions of Antarctica.

Visual inspection of vertical cloud profiles during a case study suggests that RA1M_mod reproduces the observed cloud vertical structure most closely. All model configurations over-estimate ice concentrations in a mid-level Altostratus layer (between ~3-5 km) and under-estimate liquid concentrations throughout the atmosphere, although this is especially visible at lower levels (below ~2 km). RA1M_mod produces the second lowest ice mass mixing ratios above 3 km and twice as much liquid as the next-best configuration in a lower layer, bringing the modelled cloud liquid mass mixing ratio closer to observed values.

By improving the MetUM's representation of cloud phase in a case study, RA1M_mod restricts biases in downwelling radiative fluxes to around 5% of their observed values. The resultant net radiation bias of 10.83 W m^{-2} is almost half that of 20.23 W m^{-2} produced by the default RA1M configuration. During the whole OFCAP period, only the model's representation of surface fluxes was evaluated because continuous observations of cloud properties were not available. Biases in

434 downwelling radiative fluxes during the OFCAP period were less than 8% of their observed values,
435 which produced a net radiation bias of -7.32 W m^{-2} (11%). RA1M_mod is able to simulate the
436 occurrence and magnitude of summertime melt better than the versions of the MetUM used in
437 previous studies, such as K15, which used the default Smith (1990) large-scale cloud scheme without
438 the modifications noted here. Over the entire OFCAP period, we find a mean bias of -1.72 W m^{-2} in
439 modelled melt flux at AWS14, which represents a four-fold reduction on the bias of 7.6 W m^{-2}
440 reported by K15. Despite this improvement, further developments in the representation of cloud
441 phase are evidently still needed to reduce summertime biases in melt. Observed cumulative
442 meltwater production of 114 mm (water equivalent) during the OFCAP period is still underestimated
443 by 13% due to errors in the modelled SEB. Biases of 4.59 W m^{-2} and 6.35 W m^{-2} in the latent and
444 sensible heat fluxes, respectively, account for a large proportion of the overall biases in E_{tot} and are
445 greater than those shown in K15. Remaining sources of error likely includes model schemes beyond
446 the scope of this paper, such as the land surface, snow or boundary layer schemes.

447 The RA1M setup likely outperforms the RA1T configurations because it has been more extensively
448 developed, and is designed for use in colder mid-latitude conditions, that are more comparable to
449 those observed in the Antarctic, and because it is based on the Smith (1990) large-scale cloud
450 scheme, which has been more extensively modified and tested than the prognostic PC2 scheme on
451 which RA1T is based. RA1T probably requires further development before it is suitable for use in
452 the Antarctic environment. Additionally, the superior performance of RA1M_mod over the basic
453 RA1M setup supports the findings of previous work that modifications to increase the amount of
454 liquid and limit its conversion to ice improve the representation of cold mixed-phase clouds (Furtado
455 & Field 2017; Abel et al. 2019). These modifications may also be compatible with the MetUM's
456 double-moment microphysics scheme, which is currently in development, although this requires
457 further investigation. The RA1M_mod configuration will improve simulations of surface melting and
458 ice shelf change in this rapidly changing environment, and, in future work, we will use RA1M_mod

to produce a multi-decadal hindcast to investigate atmospheric processes influencing the SEB and hence melting of Antarctic Peninsula ice shelves.

Acknowledgements

The authors confirm that they have no conflicts of interest to declare. This work was supported by the Natural Environment Research Council through the EnvEast Doctoral Training Partnership [grant number NE/L002582/1]. The authors also acknowledge use of the MONSooN system, a collaborative facility supplied under the Joint Weather and Climate Research Programme, a strategic partnership between the Met Office and the Natural Environment Research Council. The authors gratefully acknowledge the comments of two anonymous reviewers, which considerably strengthened the study.

Data availability

Model data are available from the UK Met Office Managed Archive Storage System (MASS). AWS data can be retrieved from https://www.projects.science.uu.nl/iceclimate/aws/. Aircraft data are available from the British Atmospheric Data Centre, cited as: Natural Environment Research Council; Lachlan-Cope, T.; Elvidge, A.D.; Smith, V.; Kirchgaessner, A.; King, J.C.; Ladkin, R. (2014): British Antarctic Survey Twin Otter aircraft Meteorological Airborne Science INstrumentation (MASIN) core data from the Orographic Flows and the Climate of the Antarctic Peninsula (OFCAP) project (2011). NCAS British Atmospheric Data Centre, 24 September 2014. doi:10.5285/2f53b18d-49fc-4477-b994-f1719d6f6dbe.

Appendix A: Aircraft instrumentation and data treatment

Cloud microphysics are observed using the British Antarctic Survey's instrumented De Haviland Twin Otter aircraft, which measures standard meteorological variables: total temperature is measured with Rosemount probes, static pressure is measured using in-built aircraft sensors, humidity is observed by a Vaisala humicap sensor and cooled mirror hygrometer, and three dimensional winds are measured using a Best Aircraft Turbulence (BAT) probe (Crawford & Dobosy, 1992), mounted on a boom fitted to the nose of the aircraft. Upwelling and downwelling radiative fluxes (shortwave and longwave) are measured using Eppley pyranometers and pyrgeometers mounted to the belly and roof of the aircraft, respectively. Surface temperatures are measured using a downward-looking infrared thermometer (Heitronics KT19.82). A full description of the aircraft's instrumentation can be found in King et al. (2008). The aircraft can be adapted to measure specific areas of interest, and during the OFCAP campaign was fitted with a Droplet Measurement Technologies Cloud, Aerosol and Precipitation Spectrometer (CAPS probe, Baumgardner et al., 2001) to sample cloud properties. The probe contains three separate instruments: a Cloud and Aerosol Spectrometer (CAS) which measures the diameter of small cloud particles 0.5 - 50 μm, a Cloud Imaging Probe, (CIP), which images larger cloud and precipitation-sized particles of 25 μm - 1.5 mm diameter using a charge-coupled device array, and a hotwire liquid water contents (LWC) sensor, which is used to validate CAS data.

In-cloud particles observed by the CAS instrument are all assumed to be liquid droplets, whereas those observed by the CIP must be post-processed to determine their phase. After data are quality controlled and processed using the method of Crosier et al. (2011), cloud particles are segregated into ice and liquid using the technique of Lachlan-Cope et al. (2016) by determining their circularity, C, defined as:

$$C = P^2/4\,\pi\,A \qquad \text{(A1)}$$

where P is the particle perimeter as measured by the instrument and A is the particle area, which must be a minimum of 50 pixels (or ~200 μm) to be detected. Particles with $0.9 \leq C \leq 1.2$ are considered to be circular and are thus classified as drops, while those with $C \geq 1.4$ are classified as ice. Following visual inspection of the data from the flights considered, particles with intermediate circularity $1.2 \leq C \leq 1.4$ are classified as ice, as in Lachlan-Cope et al. (2016). Ice water contents are then calculated with the mass-dimensional relationship of Brown & Francis (1995).

Only in-cloud data are used to compute mean profiles, where cloud is defined as in Lachlan-Cope et al. (2016) when the CAS instrument measures either number concentrations above 1 cm^{-3} of droplet-sized particles greater than 1 μm in diameter or when the CIP instrument measures number concentrations of ice particles above 1.0×10^{-8} cm^{-3}.

Appendix B: Automatic Weather Station (AWS) data

Observations of surface energy fluxes and meteorology are retrieved from the Larsen North automatic weather station (AWS14), which is set up as described in Kuipers Munneke et al. (2009). Observations of air temperature, pressure, relative humidity, wind speed and direction, and radiative fluxes (up- and downwelling components of longwave and shortwave) are made directly, while the sensible and latent heat fluxes are calculated using the bulk aerodynamic method. An energy balance model (van den Broeke et al., 2005) is applied to compute the energy balance of the snowpack after the raw data have been corrected using the method of Kuipers Munneke et al. (2012).

Appendix C: Numerical weather prediction model description and parameterisation schemes

The Met Office Unified Model (MetUM) is a numerical weather prediction model used for operational and research purposes. Its dynamical core is non-hydrostatic and uses semi-implicit

timestepping and semi-Lagrangian advection (Walters et al., 2017). Model equations are solved on a staggered Arakawa-C grid in the horizontal and with Charney-Phillips staggering in the vertical, with a hybrid height vertical coordinate that is terrain-following near the surface. It is run in atmosphere-only mode and configured similarly to Orr et al. (2014), although in contrast to that work, this study uses just one nested domain at 1.5 km horizontal grid spacing with a 60 second time step. This inner nest takes input from a global model that has ~17 km resolution in the mid-latitudes, which is forced at the boundaries with Met Office global operational analyses.

Simulations are run in forecast mode as described in the main text: re-initialisations occur at 0000 UTC and 1200 UTC, with only the t+12 to t+24 part of the forecast retained. The case study is initialised 12 hours prior to the flight, while the OFCAP simulation comprises a series of forecasts concatenated together. All quantities of interest are outputted as instantaneous values every 15 minutes, except meteorological variables, which are outputted hourly. During the OFCAP period, all variables are outputted as hourly instantaneous values.

The radiation scheme (SOCRATES) is based on Edwards & Slingo (1996), which calculates surface radiative fluxes prognostically using six shortwave and nine longwave absorption bands. Absorption and scattering by cloud particles are treated by applying "thick averaging" to calculate droplet effective radius from number concentrations computed by the microphysics, and ice crystals are parameterised according to Baran et al. (2016).

The operational single-moment microphysics scheme used in all experiments is based on Wilson & Ballard (1999) and represents condensate mass mixing ratios only, with prescribed number concentrations over land (including ice shelves) and open water. The scheme is three-phase, representing cloud liquid water, rain and snow (which encompasses all ice in the gridbox) prognostically. Microphysical processes produce or deplete condensate in each layer as follows: liquid droplets are formed via condensation, and are removed by droplet settling, autoconversion to

553 rain drops, freezing during the ice nucleation process and riming. Rain droplets form from cloud
554 water via autoconversion, from cloud water or other rain droplets via sedimentation or accretion, and
555 from ice by melting. Rain is depleted by sedimentation or evaporation, or converted into ice during
556 homogeneous ice nucleation or ice crystal capture. Ice is produced directly from the vapour phase via
557 vapour diffusion (the Wegener-Bergeron-Findeisen process), or from the liquid phase via rain
558 droplet capture or riming, and is lost due to sedimentation, sublimation and melting. Heterogeneous
559 ice nucleation occurs when the temperature is below a specified threshold and liquid water is present
560 in a gridbox, representing an immersion freezing or condensation mechanism. All experiments use a
561 modified threshold of -18°C rather than the default -10°C, as this modification was shown by Field et
562 al. (2014) to improve the representation of mixed-phase cloud because it forces supercooled liquid to
563 remain liquid at colder temperatures.

564

565 **References**

566 Abel, S. J., Walters, D. N., & Allen, G. (2010). Evaluation of stratocumulus cloud prediction in the
567 Met Office forecast model during VOCALS-REx. Atmospheric Chemistry and Physics, 10(21),
568 10541–10559. https://doi.org/10.5194/acp-10-10541-2010

569 Abel, S. J., Boutle, I. A., Waite, K., Fox, S., Brown, P. R. A., Cotton, R., Lloyd, G., Choularton, T.
570 W. & Bower, K. N. (2017). The Role of Precipitation in Controlling the Transition from
571 Stratocumulus to Cumulus Clouds in a Northern Hemisphere Cold-Air Outbreak. Journal of the
572 Atmospheric Sciences, 74(7), 2293–2314. https://doi.org/10.1175/JAS-D-16-0362.1

573 Agosta, C., Amory, C., Kittel, C., Orsi, A., Favier, V., Gallée, H., van den Broeke, M. R., Lenaerts,
574 J. T. M., van Wessem, J. M. & Fettweis, X. (2018). Estimation of the Antarctic surface mass balance
575 using MAR (1979-2015) and identification of dominant processes. The Cryosphere Discussions, (D),
576 1–22. https://doi.org/10.5194/tc-2018-76

577 Baran, A. J., Hill, P., Furtado, K., Field, P., & Manners, J. (2014). A Coupled Cloud Physics –
578 Radiation Parameterization of the Bulk Optical Properties of Cirrus and Its Impact on the Met Office
579 Unified Model Global. Journal of Climate, 27(20), 7725–7752. https://doi.org/10.1175/JCLI-D-13-
580 00700.1

581 Barrett, A. I., Hogan, R. J., & Forbes, R. M. (2017). Why are mixed-phase altocumulus clouds
582 poorly predicted by large-scale models? Part 1. Physical processes. Journal of Geophysical Research:
583 Atmospheres, 122(18), 9903–9926. https://doi.org/10.1002/2016JD026321

584 Baumgardner, D., Jonsson, H., Dawson, W., O'Connor, D., & Newton, R. (2001). The cloud, aerosol
585 and precipitation spectrometer: A new instrument for cloud investigations. Atmospheric Research,
586 59–60, 251–264. https://doi.org/10.1016/S0169-8095(01)00119-3

587 Bennartz, R., Shupe, M. D., Turner, D. D., Walden, V. P., Steffen, K., Cox, C. J., Kulie, M. S.,
588 Miller, N. B. & Pettersen, C. (2013). July 2012 Greenland melt extent enhanced by low-level liquid
589 clouds. Nature, 496(7443), 83–86. https://doi.org/10.1038/nature12002

590 Bevan, S., Luckman, A., Hubbard, B., Kulessa, B., Ashmore, D., Kuipers Munneke, P., Leary, M.
591 O., Booth, A., Sevestre, H. & McGrath, D. (2017). Centuries of intense surface melt on Larsen C Ice
592 Shelf. The Cryosphere Discussions, 1–21. https://doi.org/10.5194/tc-2017-81

593 Bodas-Salcedo, A., Williams, K. D., Field, P. R., & Lock, A. P. (2012). The surface downwelling
594 solar radiation surplus over the southern ocean in the met office model: The role of midlatitude
595 cyclone clouds. Journal of Climate, 25(21), 7467–7486. https://doi.org/10.1175/JCLI-D-11-00702.1

596 Bromwich, D. H., Nicolas, J. P., Hines, K. M., Kay, J. E., Key, E. L., Lazzara, M. A., Lubin, D.,
597 McFarquhar, G. M., Gorodetskaya, I. V., Grosvenor, D. P., Lachlan-Cope, T. & Van Lipzig, N. P.
598 M. (2012). Tropospheric clouds in Antarctica. Reviews of Geophysics, 50(1), 1–40.
599 https://doi.org/10.1029/2011RG000363

Bromwich, D. H., Otieno, F. O., Hines, K. M., Manning, K. W., & Shilo, E. (2013). Comprehensive evaluation of polar weather research and forecasting model performance in the antarctic. Journal of Geophysical Research Atmospheres, 118(2), 274–292. https://doi.org/10.1029/2012JD018139

Brown, P. R. A., & Francis, P. N. (1995). Improved measurements of the ice water content in cirrus using a total-water probe. Journal of Atmospheric and Oceanic Technology, 12(4), 410–414. https://doi.org/https://doi.org/10.1175/1520-0426(1995)012<0410:IMOTIW>2.0.CO;2

Bush, M., Allen, T., Bain, C., Boutle, I., Edwards, J., Finnenkoetter, A., Franklin, C., Hanley, K., Lean, H., Lock, A., Manners, J., Mittermaier, M., Morcrette, C., North, R., Petch, J., Short, C., Vosper, S., Walters, D., Webster, S., Weeks, M., Wilkinson, J. & Wood, N. (2019). The first Met Office Unified Model / JULES Regional Atmosphere and Land configurations, RAL1. Geoscientific Model Development, in review (June), 1–48. https://doi.org/https://doi.org/10.5194/gmd-2019-130

Cook, A. J., & Vaughan, D. G. (2010). Overview of areal changes of the ice shelves on the Antarctic Peninsula over the past 50 years. The Cryosphere Discussions, 3(2), 579–630. https://doi.org/10.5194/tcd-3-579-2009

Cox, P. M., Betts, R. A., Bunton, C. B., Essery, R. L. H., Rowntree, P. R., & Smith, J. (1999). The impact of new land surface physics on the GCM simulation of climate and climate sensitivity. Climate Dynamics, 15(3), 183–203. https://doi.org/10.1007/s003820050276

Crawford, T. L. and R. J. Dobosy (1992). "A sensitive fast-response probe to measure turbulence and heat flux from any airplane." Boundary-Layer Meteorology 59(3): 257-278. https://doi.org/10.1007/BF00119816

Crosier, J., Bower, K. N., Choularton, T. W., Westbrook, C. D., Connolly, P. J., Cui, Z. Q., Crawford, I. P., Capes, G. L., Coe, H., Dorsey, J. R., Williams, P. I., Illingworth, A. J., Gallagher, M. W. & Blyth, A. M. (2011). Observations of ice multiplication in a weakly convective cell embedded

623 in supercooled mid-level stratus. Atmospheric Chemistry and Physics, 11(1), 257–273.
624 https://doi.org/10.5194/acp-11-257-2011

625 Edwards, J. M., & Slingo, A. (1996). Studies with a flexible new radiation code. I: Choosing a
626 configuration for a large-scale model. Quarterly Journal of the Royal Meteorological Society, 122,
627 689–719. https://doi.org/10.1002/qj.49712253107

628 Elvidge, A. D., Renfrew, I. A., King, J. C., Orr, A., Lachlan-Cope, T. A., Weeks, M., & Gray, S. L.
629 (2015). Foehn jets over the Larsen C Ice Shelf, Antarctica. Quarterly Journal of the Royal
630 Meteorological Society, 141(688), 698–713. https://doi.org/10.1002/qj.2382

631 Elvidge, A. D., Renfrew, I. A., King, J. C., Orr, A., & Lachlan-Cope, T. A. (2016). Foehn warming
632 distributions in nonlinear and linear flow regimes: A focus on the Antarctic Peninsula. Quarterly
633 Journal of the Royal Meteorological Society, 142(695), 618–631. https://doi.org/10.1002/qj.2489

634 Essery, R. L. H., Best, M. J., & Cox, P. M. (2001). MOSES 2.2 technical documentation. Hadley
635 Centre Technical Note 30. Retrieved from http://jules.jchmr.org/sites/default/files/HCTN_30.pdf

636 Field, P. R., Cotton, R. J., Mcbeath, K., Lock, A. P., Webster, S., & Allan, R. P. (2014). Improving a
637 convection-permitting model simulation of a cold air outbreak. Quarterly Journal of the Royal
638 Meteorological Society, 140, 124–138. https://doi.org/10.1002/qj.2116

639 Furtado, K., Field, P. R., Boutle, I. A., Morcrette, C. J., & Wilkinson, J. M. (2016). A Physically
640 Based Subgrid Parameterization for the Production and Maintenance of Mixed-Phase Clouds in a
641 General Circulation Model. Journal of the Atmospheric Sciences, 73(1), 279–291.
642 https://doi.org/10.1175/JAS-D-15-0021.1

643 Furtado, K., & Field, P. (2017). The Role of Ice Microphysics Parametrizations in Determining the
644 Prevalence of Supercooled Liquid Water in High-Resolution Simulations of a Southern Ocean

645 Midlatitude Cyclone. In Journal of the Atmospheric Sciences (Vol. 74, pp. 2001–2021).
646 https://doi.org/10.1175/JAS-D-16-0165.1

647 Grosvenor, D. P., Choularton, T. W., Lachlan-Cope, T., Gallagher, M. W., Crosier, J., Bower, K. N.,
648 Ladkin, R. S. & Dorsey, J. R. (2012). In-situ aircraft observations of ice concentrations within clouds
649 over the Antarctic Peninsula and Larsen Ice Shelf. Atmospheric Chemistry and Physics, 12(23),
650 11275–11294. https://doi.org/10.5194/acp-12-11275-2012

651 Grosvenor, D. P., Field, P. R., Hill, A. A., & Shipway, B. J. (2017). The relative importance of
652 macrophysical and cloud albedo changes for aerosol-induced radiative effects in closed-cell
653 stratocumulus: Insight from the modelling of a case study. Atmospheric Chemistry and Physics,
654 17(8), 5155–5183. https://doi.org/10.5194/acp-17-5155-2017

655 Hines, K. M., Bromwich, D. H., Wang, S. H., Silber, I., Verlinde, J., & Lubin, D. (2019).
656 Microphysics of summer clouds in central West Antarctica simulated by the Polar Weather Research
657 and Forecasting Model (WRF) and the Antarctic Mesoscale Prediction System (AMPS).
658 Atmospheric Chemistry and Physics, 19(19), 12431–12454. https://doi.org/10.5194/acp-19-12431-
659 2019

660 Hyder, P., Edwards, J. M., Allan, R. P., Hewitt, H. T., Bracegirdle, T. J., Gregory, J. M., Wood, R.
661 A., Meijers, A. J. S., Mulcahy, J., Field, P. R., Furtado, K., Bodas-Salcedo, A., Williams, K. D.,
662 Copsey, D., Josey, S. A., Liu, C., Roberts, C. D., Sanchez, C., Ridley, J., Thorpe, L., Hardiman, S.
663 C., Mayer, M., Berry, D. I. & Belcher, S. E. (2018). Critical Southern Ocean climate model biases
664 traced to atmospheric model cloud errors. Nature Communications, 9(1), 3625.
665 https://doi.org/10.1038/s41467-018-05634-2

666 Kalesse, H., de Boer, G., Solomon, A., Oue, M., Ahlgrimm, M., Zhang, D., Shupe, M. D., Luke, E.
667 & Protat, A. (2016). Understanding Rapid Changes in Phase Partitioning between Cloud Liquid and

668 Ice in Stratiform Mixed-Phase Clouds: An Arctic Case Study. Monthly Weather Review, 144(12),
669 4805–4826. https://doi.org/10.1175/MWR-D-16-0155.1

670 King, J. C., Lachlan-Cope, T. A., Ladkin, R. S., & Weiss, A. (2008). Airborne Measurements in the
671 Stable Boundary Layer over the Larsen Ice Shelf , Antarctica. Boundary Layer Meteorology, 127(3),
672 413–428. https://doi.org/10.1007/s10546-008-9271-4

673 King, J. C., Gadian, A., Kirchgaessner, A., Kuipers Munneke, P., Lachlan-Cope, T. A., Orr, A.,,
674 Reijmer, C., Van Den Broeke, M. R., Van Wessem, J. M. & Weeks, M. (2015). Validation of the
675 summertime surface energy budget of Larsen C Ice Shelf (Antarctica) as represented in three high-
676 resolution atmospheric models. Journal of Geophysical Research Atmospheres, 120(4), 1335–1347.
677 https://doi.org/10.1002/2014JD022604

678 Klein, S. A., Mccoy, R. B., Morrison, H., Ackerman, A. S., De Boer, G., Chen, M., Cole, J. N. S.,
679 Genio, D. D., Foster, M. J., Fridlind, A., Golaz, J.-c., Hashino, T., Jerry, Y., Hoose, C.,
680 Khairoutdinov, M. F., Larson, V. E., Liu, X., Mcfarquhar, G. M., Menon, S., Neggers, R. A. J., Park,
681 S., Michael, R., Schmidt, J. M., Sednev, I., Shipway, B. J., Shupe, M. D., Spangenberg, D. A., Sud,
682 Y. C., Turner, D. D., Veron, D. E., Von, K., Walker, G. K., Wang, Z., Wolf, A. B. & Xie, S. (2009).
683 Intercomparison of model simulations of mixed-phase clouds observed during the ARM Mixed-
684 Phase Arctic Cloud Experiment . I : Single-layer cloud. Quarterly Journal of the Royal
685 Meteorological Society, 1002(May), 979–1002. https://doi.org/10.1002/qj

686 Kuipers Munneke, P., van den Broeke, M. R., Reijmer, C. H., Helsen, M. M., Boot, W., Schneebeli,
687 M., & Steffen, K. (2009). The role of radiation penetration in the energy budget of the snowpack at
688 Summit, Greenland. The Cryosphere, 3(1), 155–165. https://doi.org/10.5194/tcd-3-277-2009

689 Kuipers Munneke, P., Van Den Broeke, M. R., King, J. C., Gray, T., & Reijmer, C. H. (2012). Near-
690 surface climate and surface energy budget of Larsen C ice shelf, Antarctic Peninsula. Cryosphere,
691 6(2), 353–363. https://doi.org/10.5194/tc-6-353-2012

692 Lachlan-Cope, T. (2010). Antarctic clouds. Polar Research, 29(2), 150–158.
693 https://doi.org/10.1111/j.1751-8369.2010.00148.x

694 Lachlan-cope, T., Listowski, C., & Shea, S. O. (2016). The microphysics of clouds over the
695 Antarctic Peninsula – Part 1: Observations. Atmospheric Chemistry and Physics, 16, 15605–15617.
696 https://doi.org/10.5194/acp-16-15605-2016

697 Lenaerts, J. T. M., Van Tricht, K., Lhermitte, S., & L'Ecuyer, T. S. (2017). Polar clouds and
698 radiation in satellite observations, reanalyses, and climate models. Geophysical Research Letters,
699 44(7), 3355–3364. https://doi.org/10.1002/2016GL072242

700 Lenaerts, J. T. M., Ligtenberg, S. R. M., Medley, B., van de Berg, W. J., Konrad, H., Nicolas, J. P.,
701 van Wessem, J. M., Trusel, L. D., Mulvaney, R., Tuckwell, R. J., Hogg, A. E. & Thomas, E. R.
702 (2018). Climate and surface mass balance of coastal West Antarctica resolved by regional climate
703 modelling. Annals of Glaciology, 59(76, pt1), 29–41. https://doi.org/10.1017/aog.2017.42
704 Listowski, C., & Lachlan-cope, T. (2017). The Microphysics of Clouds over the Antarctic Peninsula
705 – Part 2: modelling aspects within Polar WRF. Atmospheric Chemistry and Physics, 17, 10195–
706 10221. https://doi.org/https://doi.org/10.5194/acp-17-10195-2017
707 Listowski, C., Delanoë, J., Kirchgaessner, A., Lachlan-Cope, T., & King, J. (2019). Antarctic clouds,
708 supercooled liquid water and mixed phase, investigated with DARDAR: Geographical and seasonal
709 variations. Atmospheric Chemistry and Physics, 19(10), 6771–6808. https://doi.org/10.5194/acp-19-
710 6771-2019

711 Lock, A. (2011). Stable boundary layer modelling at the Met Office. In: ECMWF GABLS workshop
712 (pp. 7–10).

713 Miller, N. B., Shupe, M. D., Cox, C. J., Walden, V. P., Turner, D. D., & Steffen, K. (2015). Cloud
714 radiative forcing at Summit, Greenland. Journal of Climate, 28(15), 6267–6280.
715 https://doi.org/10.1175/JCLI-D-15-0076.1

716 Nicolas, J. P., Vogelmann, A. M., Scott, R. C., Wilson, A. B., Cadeddu, M. P., Bromwich, D. H.,
717 Verlinde, J., Lubin, D., Russell, L. M., Jenkinson, C., Powers, H. H., Ryczek, M., Stone, G. Wille, J.
718 D. (2017). January 2016 extensive summer melt in West Antarctica favoured by strong El Niño.
719 Nature Communications, 8(May), 1–10. https://doi.org/10.1038/ncomms15799
720 Orr, A., Phillips, T., Webster, S., Elvidge, A., Weeks, M., Hosking, S., & Turner, J. (2014). Met
721 Office Unified Model high-resolution simulations of a strong wind event in Antarctica. Quarterly
722 Journal of the Royal Meteorological Society, 140(684), 2287–2297. https://doi.org/10.1002/qj.2296

723 Scambos, T. A., Hulbe, C., M.Fahnestock, & J.Bohlander. (2000). The link between climate
724 warming and break-up of ice shelves in the Antarctica Peninsula. Journal of Glaciology, 46(154),
725 516–530. https://doi.org/10.3189/172756500781833043

726 Scambos, T., Hulbe, C., & Fahnestock, M. (2003). Climate-induced ice shelf disintegration in the
727 Antarctic Peninsula. In E. Domack, A. Levente, A. Burnet, R. Bindschadler, P. Convey, & M. Kirby
728 (Eds.), Antarctic Peninsula Climate Variability: Historical and Paleoenvironmental Perspectives
729 (Vol. 79, pp. 79–92). https://doi.org/doi:10.1029/AR079p0079

730 Smith, R. N. B. (1990). A scheme for predicting layer clouds and their water content in a general
731 circulation model. Quarterly Journal of the Royal Meteorological Society, 116, 435–460.
732 https://doi.org/10.1002/qj.49711649210

733 Souverijns, N., Gossart, A., Demuzere, M., Lenaerts, J. T. M., Medley, B., Gorodetskaya, I. V.,
734 Vanden Broucke, S. & van Lipzig, N. P. M. (2019). A New Regional Climate Model for POLAR-
735 CORDEX: Evaluation of a 30-Year Hindcast with COSMO-CLM 2 over Antarctica. Journal of
736 Geophysical Research: Atmospheres, 124(3), 1405–1427. https://doi.org/10.1029/2018JD028862

737 Tan, I., & Storelvmo, T. (2016). Sensitivity Study on the Influence of Cloud Microphysical
738 Parameters on Mixed-Phase Cloud Thermodynamic Phase Partitioning in CAM5. Journal of the
739 Atmospheric Sciences, 73(2), 709–728. https://doi.org/10.1175/JAS-D-15-0152.1

740 Turner, J., Colwell, S. R., Marshall, G. J., Lachlan-Cope, T. A., Carleton, A. M., Jones, P. D., Lagun,
741 V., Reid, P. A. & Iagovkina, S. (2005). Antarctic climate change during the last 50 years.
742 International Journal of Climatology, 25(3), 279–294. https://doi.org/10.1002/joc.1130

743 Turner, J., Lu, H., White, I., King, J. C., Phillips, T., Hosking, J. S., Bracegirdle, T. J., Marshall, G.,
744 J., Mulvaney, Robert & Deb, P. (2016). Absence of 21st century warming on Antarctic Peninsula
745 consistent with natural variability. Nature, 535(7612), 411–415. https://doi.org/10.1038/nature18645

746 van den Broeke, M. (2005). Strong surface melting preceded collapse of Antarctic Peninsula ice
747 shelf. Geophysical Research Letters, 32, 2–5. https://doi.org/10.1029/2005GL023247

748 van den Broeke, M. R., Reijmer, C., Van As, D., Van de Wal, R., & Oerlemans, J. (2005). Seasonal
749 cycles of Antarctic surface energy balance from automatic weather stations. Annals of Glaciology,
750 41(Aws 4), 131–139. https://doi.org/10.3189/172756405781813168

751 Van Wessem, J. M., Reijmer, C. H., Lenaerts, J. T. M., van de Berg, W. J., van den Broeke, M. R., &
752 Van Meijgaard, E. (2014). Updated cloud physics in a regional atmospheric climate model improves
753 the modelled surface energy balance of Antarctica. Cryosphere, 8(1), 125–135.
754 https://doi.org/10.5194/tc-8-125-2014

755 Van Wessem, J. M., van de Berg, W. J., Noël, B. P. Y., van Meijgaard, E., Birnbaum, G., Jakobs, C.
756 L., Krüger, K., Lenaerts, J. T. M., Lhermitte, S., Ligtenberg, S. R. M., Medley, B., Reijmer, C. H.,
757 van Tricht, K., Trusel, L. D., van Ulft, L. H., Wouters, B., Wuite, J. & van den Broeke, M. R. (2018).
758 Modelling the climate and surface mass balance of polar ice sheets using RACMO2, part 2:
759 Antarctica (1979-2016). The Cryosphere, 12, 1479–1498. https://doi.org/10.5194/tc-2017-202

760 Vergara-Temprado, J., Miltenberger, A. K., Furtado, K., Grosvenor, D. P., Shipway, B. J., Hill, A.
761 A., Wilkinson, J. M., Field, P. R., Murray, B. J. & Carslaw, K. S. (2018). Strong control of Southern
762 Ocean cloud reflectivity by ice-nucleating particles. Proceedings of the National Academy of
763 Sciences, 115(11), 2687–2692. https://doi.org/10.1073/pnas.1721627115

764 Walters, D., Boutle, I., Brooks, M., Melvin, T., Stratton, R., Vosper, S., Wells, H., Williams, K.,
765 Wood, N., Allen, T., Bushell, A., Copsey, D., Earnshaw, P., Edwards, J., Gross, M., Hardiman, S.,
766 Harris, C., Heming, J., Klingaman, N., Levine, R., Manners, J., Martin, G., Milton, S., Mittermaier,
767 M., Morcrette, C., Riddick, T., Roberts, M., Sanchez, C., Selwood, P., Stirling, A., Smith, C., Suri,
768 D., Tennant, W., Luigi Vidale, P., Wilkinson, J., Willett, M., Woolnough, S. & Xavier, P. (2017).
769 The Met Office Unified Model Global Atmosphere 6.0/6.1 and JULES Global Land 6.0/6.1
770 configurations. Geoscientific Model Development, 10(4), 1487–1520. https://doi.org/10.5194/gmd-
771 10-1487-2017

772 Wilson, D. R., & Ballard, S. P. (1999). A microphysically based precipitation scheme for the UK
773 Meteorological Office Unified Model. Quarterly Journal of the Royal Meteorological Society,
774 125(557), 1607–1636. https://doi.org/10.1002/qj.49712555707

775 Wilson, D. R., Bushell, A. C., Kerr-Munslow, A. M., Price, J. D., & Morcrette, C. J. (2008). PC2: A
776 prognostic cloud fraction and condensation scheme. I: Scheme description. Quarterly Journal of the
777 Royal …, 134(October), 2093–2107. https://doi.org/10.1002/qj

778 Zhang, T., Stamnes, K., & Bowling, S. A. (1996). Impact of Clouds on Surface Radiative Fluxes and
779 Snowmelt in the Arctic and Subarctic. *Journal of Climate*, *9*(9), 2110–2123.
780 https://doi.org/10.1175/1520-0442(1996)009<2110:IOCOSR>2.0.CO;2

781

782

783

784

785

786

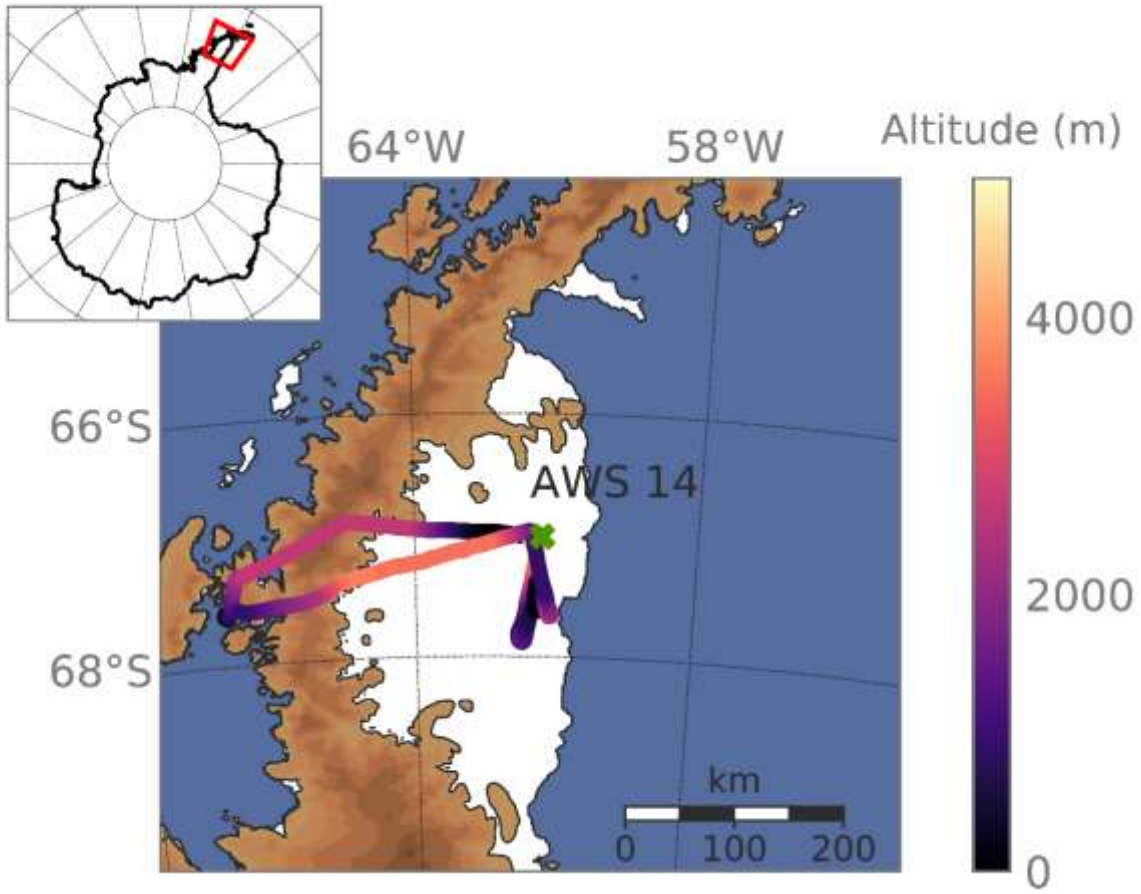

Figure 1 - The inner 1.5 km resolution MetUM model domain used in this study, centred on Larsen C Ice Shelf. The model's surface elevation is indicated by shaded contours. The flight track of the f152 case study is also shown, where the aircraft's altitude is indicated by the scale shown on the right, and the location of AWS14 is marked with a cross. The inset map shows the location of the model domain in a wider Antarctic context.

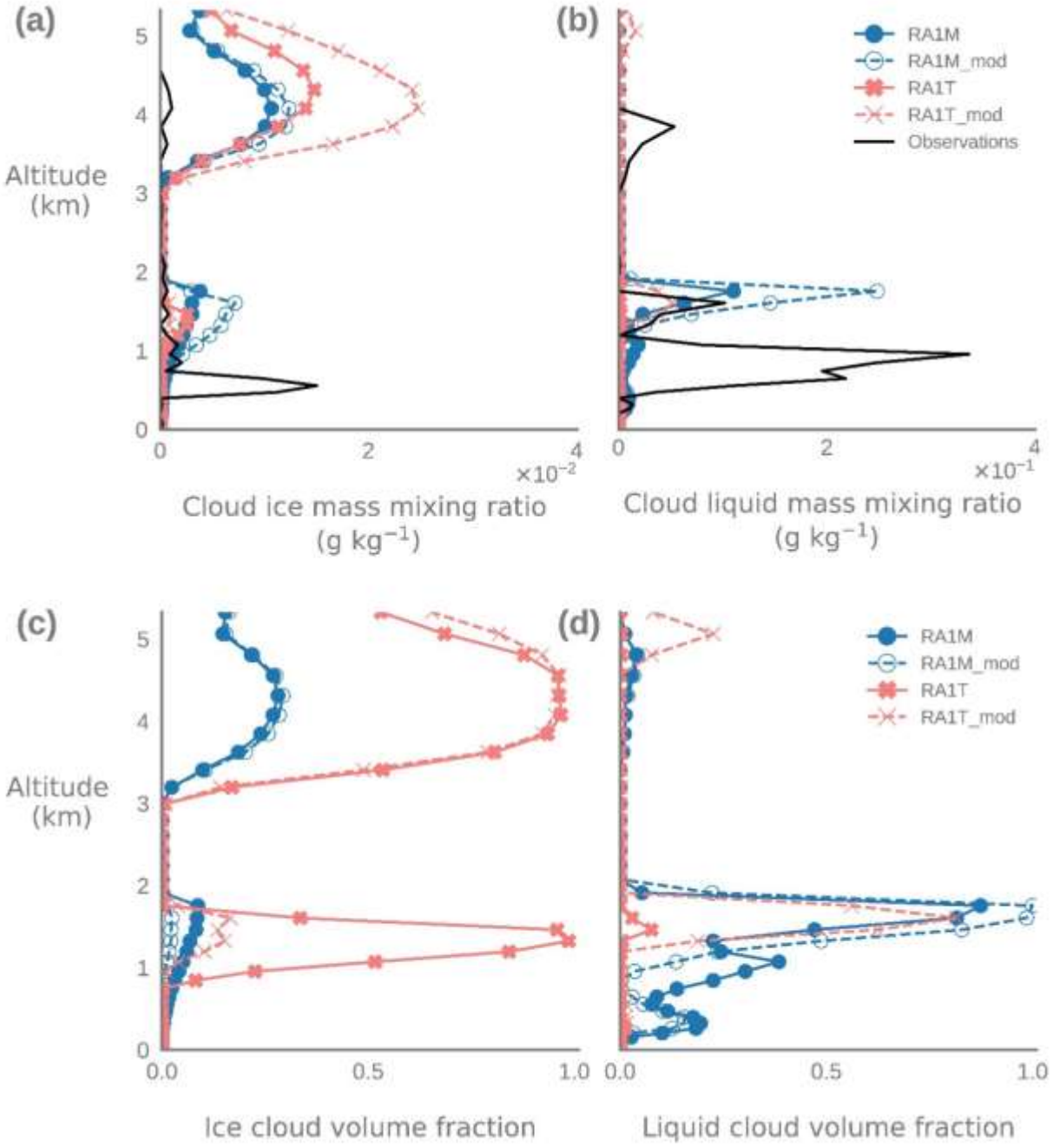

Figure 2 - Mean vertical profiles of cloud a) ice and b) liquid mass mixing ratios, in g kg^{-1}, and mean modelled cloud gridbox volume fractions of c) ice cloud and d) liquid cloud during f152 when the aircraft was sampling over Larsen C. Observations are shown in a) and b) with the solid black line and model output above AWS14 is shown in all panels with coloured lines with markers. Solid lines

with heavy markers indicate the two 'base' configurations, while dashed lines with lighter markers show their modified counterparts. The experimental configurations are detailed in Table 1.

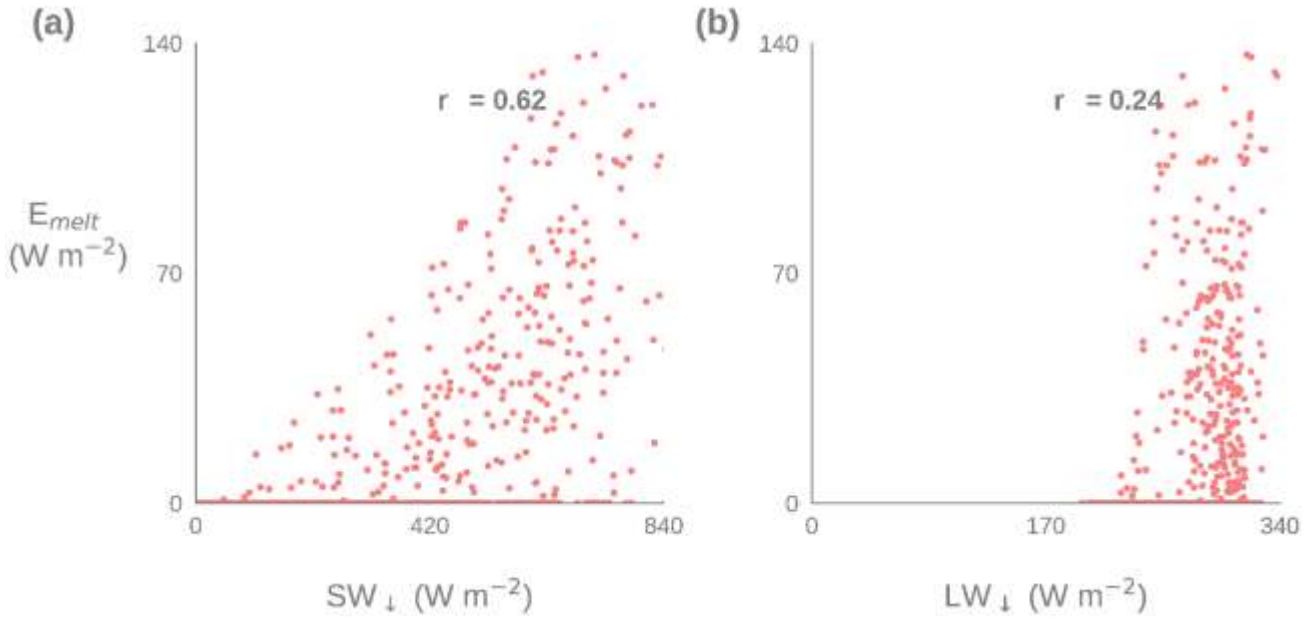

Figure 3 - Scatterplots of observed energy available for melting (E_{melt}) against a) downwelling shortwave ($SW_\downarrow$) and b) downwelling longwave ($LW_\downarrow$) at AWS14. Data plotted are instantaneous values outputted at 30-minute intervals. Pearson correlation coefficients, significant at the 99% level, are given at top centre of each panel.

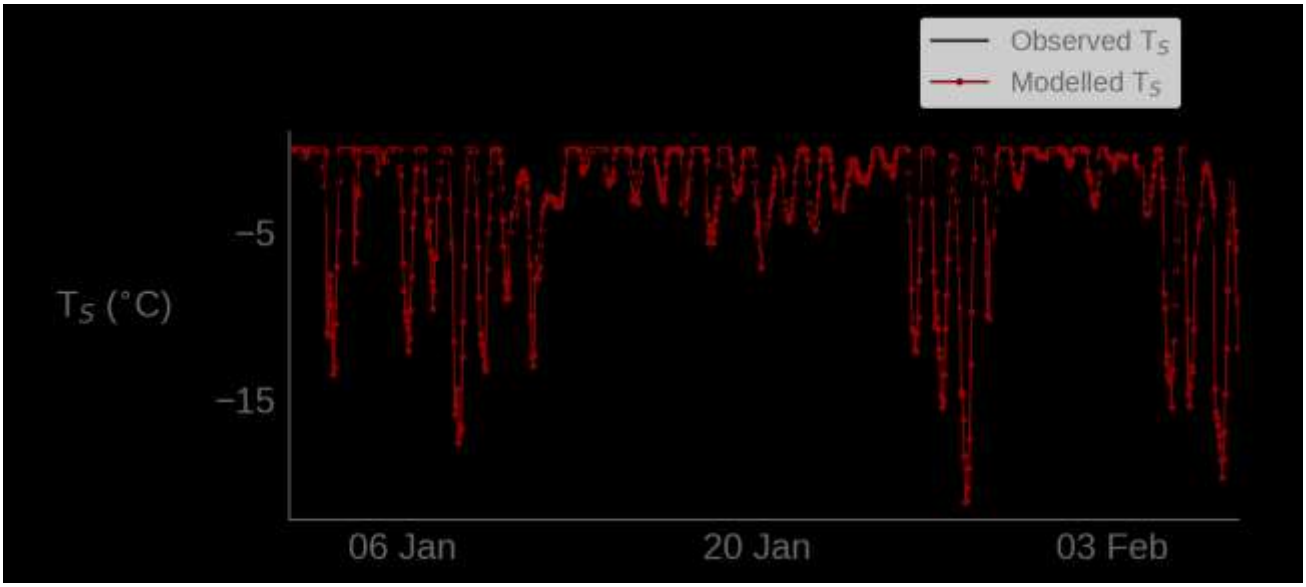

Figure 4 – Hourly surface temperature (T_s) at AWS14 during the OFCAP period. Observations are given in black, while model output is shown with filled markers.

Table 1 – Configurations for model experiments used in this study.

Experiment name	**Options**
RA1M	• RA1M physics, based on Smith (1990) large-scale cloud scheme • Heterogeneous nucleation temperature threshold set to -18°C (Field et al., 2014)
RA1M_mod	As in RA1M, with the following modifications: • Shape-dependent riming (Furtado & Field, 2017) • Modified ice cloud fraction parameterisation (Abel et al., 2017)
RA1T	• RA1T physics, based on PC2 (Wilson et al., 2008) large-scale cloud scheme • Heterogeneous nucleation temperature threshold set to -18°C (Field et al., 2014)
RA1T_mod	As in RA1T, with the following modifications: • Turbulent production of supercooled water (Furtado et al., 2016) • Shape-dependent riming (Furtado & Field, 2017)

841

842

843 *Table 2* – Time mean observed surface energy fluxes and model biases of each experiment at
844 AWS14 during f152. All fluxes are given in W m^{-2}, and are abbreviated as in Equation 1. Fluxes and
845 biases are positive when directed towards the surface. The smallest biases are highlighted in bold
846 text.

	AWS14	Mean bias			
	(observed)	RA1M	RA1M_mod	RA1T	RA1T_mod
$SW_{\downarrow}$	594.58	66.14	**30.26**	195.38	114.84
$SW_{\uparrow}$	-501.34	-55.39	**-32.06**	-135.05	-84.90
SW_{net}	93.24	10.73	**-1.80**	60.33	29.95
$LW_{\downarrow}$	279.11	9.21	12.37	-41.13	**-5.11**
$LW_{\uparrow}$	-315.64	0.28	**0.25**	0.79	0.43
LW_{net}	-36.53	9.50	12.63	-40.34	**-4.68**
H_S	-3.63	**-2.37**	-3.49	-8.62	-6.62
H_L	-10.85	7.78	7.87	**1.40**	6.21
E_{tot}	42.23	25.05	**13.15**	15.29	23.35
E_{melt}	47.31	17.33	**6.09**	9.63	16.52

847

848

849

850

851

852

853

854 *Table 3* - Pearson correlation coefficients between cloud cover, downwelling longwave ($LW_{\downarrow}$) and
855 shortwave fluxes ($SW_{\downarrow}$), and melt flux, (E_{melt}), at AWS14 during January 1 – February 7, 2011.
856 Correlation coefficients between observed components are shown in panel a), while modelled
857 coefficients are given in panel b). Correlation coefficients in bold text are significant at the 99%
858 level.

	(a) Observed correlations				**(b)** **Modelled correlations**			
	Cloud cover	$LW_{\downarrow}$	$SW_{\downarrow}$	E_{melt}	Cloud cover	$LW_{\downarrow}$	$SW_{\downarrow}$	E_{melt}
Cloud cover	1.00	-	**-0.19**	**0.12**	1.00	**0.87**	**-0.14**	**0.05**
$LW_{\downarrow}$		1.00	-	**0.24**		1.00	-	**0.15**
$SW_{\downarrow}$			1.00	**0.62**			1.00	**0.65**
E_{melt}				1.00				1.00

859

860

861

862

863

864

865 *Table 4* - Mean observed surface energy fluxes at AWS14 and mean model biases of each
866 experiment during the OFCAP period, as in Table 2. Mean biases reported by K15 are given in the

867 third column, and mean biases, RMSEs and Pearson correlation coefficients of the OFCAP
868 simulation are given in columns four to six. As in Table 2, the smallest biases are highlighted in
869 bold, and fluxes and biases are positive when directed towards the surface.

	Mean bias				
	AWS14 (observed)	K15	RA1M_mod	RMSE	Correlation coefficient
$SW_{\downarrow}$	277.86	-31.6	**-20.95**	105.03	0.91
$SW_{\uparrow}$	-232.69	41.0	**12.78**	87.78	0.91
SW_{net}	45.17	9.4	**-8.16**	24.88	0.85
$LW_{\downarrow}$	280.10	-7.0	**-0.33**	33.01	0.49
$LW_{\uparrow}$	-303.88	-2.0	**1.17**	14.12	0.63
LW_{net}	-23.79	-6.3	**0.84**	25.70	0.47
H_L	-5.11	**1.9**	4.59	8.70	0.71
H_S	-9.34	**5.9**	6.35	11.46	0.48
E_{tot}	-1.43	**10.5**	11.98	31.71	0.78
E_{melt}	13.53	7.6	**-1.72**	16.26	0.82

870